Biophysical Journal Volume: 00 Month Year 1–12

Steric Effects Induce Geometric Remodeling of Actin Bundles in Filopodia

Ulrich Dobramysl[*] Garegin A. Papoian[†‡] and Radek Erban[§‡]

Abstract

Filopodia are ubiquitous finger-like protrusions, spawned by many eukaryotic cells, to probe and interact with their environments. Polymerization dynamics of actin filaments, comprising the structural core of filopodia, largely determine their instantaneous lengths and overall lifetimes. The polymerization reactions at the filopodial tip require transport of G-actin, which enter the filopodial tube from the filopodial base and diffuse towards the filament barbed ends near the tip. Actin filaments are mechanically coupled into a tight bundle by cross-linker proteins. Interestingly, many of these proteins are relatively short, restricting the free diffusion of cytosolic G-actin throughout the bundle and, in particular, its penetration into the bundle core. To investigate the effect of steric restrictions on G-actin diffusion by the porous structure of filopodial actin filament bundle, we used a particle-based stochastic simulation approach. We discovered that excluded volume interactions result in partial and then full collapse of central filaments in the bundle, leading to a hollowed-out structure. The latter may further collapse radially due to the activity of cross-linking proteins, hence producing conical shaped filament bundles. Interestingly, electron microscopy experiments on mature filopodia indeed frequently reveal actin bundles that are narrow at the tip and wider at the base. Overall, our work demonstrates that excluded volume effects in the context of reaction-diffusion processes in porous networks may lead to unexpected geometric growth patterns and complicated, history-dependent dynamics of intermediate meta-stable configurations.

Received

Correspondence:

arXiv:1605.03119v1 [q-bio.SC] 10 May 2016

1 INTRODUCTION

Many eukaryotic cells project dynamic finger-like protrusions, called filopodia, that are comprised of a bundle of actin filaments enveloped by the cellular membrane (1, 2). Filopodia play diverse roles across many cell types. In particular, signaling via receptors on filopodial tips allows cells to sense their environment and guide chemotaxis (3). Neurons use filopodia in axonal growth cones, to determine the direction of elongation and branching (4), as well as in dendritic spine formation (5). During wound healing, "knitting" of filopodia protruding from epithelial cells plays an important role (6). Filopodia are also implicated in cancer progression and metastasis because of their involvement with cell motility (7). They also arise in some viral infections, creating physical connections among the hosts' cells (8).

G-actin, an abundant and highly conserved protein, self-assembles into double helical filaments, called F-actin. The latter is the fundamental building block of eukaryotic cellular cytoskeletons. F-actin structure is polarized, with polymerization at the barbed end being more efficient by an order of magnitude compared to the pointed end, while having similar depolymerisation rates at both ends. This asymmetry, based on the hydrolysis of ATP into ADP by actin molecules, leads to "treadmilling", whereby filaments can convert chemical energy stored in ATP into mechanical work of pushing against the external resistance. Hence, actin filaments are dynamic, dissipative structures, that allow for fast morphological transitions in the cellular cytoskeleton in response to external and internal biochemical and mechanical cues, mediated by a vast array of signaling and regulatory proteins.

In filopodia, which are roughly cylindrical tubes with radius $R \sim 50 - 250\,\mathrm{nm}$ (11, 12), between 10 and 30 actin filaments are organized into parallel, tightly cross-linked structures (see Fig. 1). The filopodial lengths, L, vary considerably between cell types, ranging from a few up to

[*]Wellcome Trust/Cancer Research UK Gurdon Institute, University of Cambridge, Tennis Court Road, Cambridge CB2 1QN, United Kingdom; e-mail: ulrich.dobramysl@gurdon.cam.ac.uk.

[†]Department of Chemistry & Biochemistry, University of Maryland, Chemistry Bldg 2216, College Park, MD 20742-2021, United States; e-mail: gpapoian@umd.edu.

[‡]G.A.P. and R.E. are joint corresponding authors.

[§]Mathematical Institute, University of Oxford, Radcliffe Observatory Quarter, Woodstock Road, Oxford, OX2 6GG, United Kingdom; e-mail: erban@maths.ox.ac.uk.

© 2015 The Authors
0006-3495/08/09/2624/12 $2.00

doi:

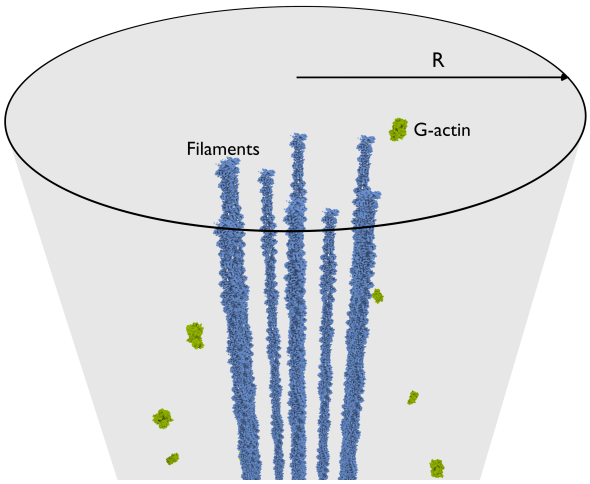

Figure 1: *Rendering of an actin filament bundle inside a filopodium. The filaments are shown in blue, with diffusing G-actin monomers displayed in green. The gray region indicates the volume enclosed by the membrane in our model. The filament height and G-actin position data stem from an example simulation run. Filament and G-actin structure data were taken from the PDBe database* (9, 10).

several tens of microns (13, 14). Many proteins are involved in the complex machinery responsible for the formation and subsequent biological function of filopodial protrusions, including formins (15), ENA/VASP (16) and capping proteins (17), among others, however, how these proteins regulate the growth-retraction dynamics of filopodia is still not fully understood (1, 18–20).

In a series of works, Papoian and coworkers have proposed a theory for length regulation in filopodia (21, 22). For a stationary filopodium, the key idea is to match three actin fluxes: the consumption of G-actin at the filopodial tip, J_p, must equal the transport or diffusional flux of G-actin to the tip, J_d, and the flux of actin subunits leaving the filopodial tube, J_r, due to retrograde flow. The latter process is mechanically mediated by the polymerization of actin against the resistance of the filopodial membrane and, to a larger extent, by contractile dynamics of actin network inside the cell body, to which the roots of filopodial actin bundles are anchored (20, 23–27). In the mean-field limit, the equations, $J_p = J_d = J_r$, can be solved to yield a closed form expression for the stationary length of filopodia (21). Prior models also investigated filopodial growth dynamics, using somewhat different assumptions and computational approaches (11, 13, 28). Detailed stochastic models of filopodial growth that included important regulatory proteins such as capping proteins, resulted in macroscopic length fluctuations of filopodial protrusions reminiscent of ubiquitously observed filopodial growth-retraction cycles (22). These near critical length fluctuations arise from the amplification of molecular noise due to binding and unbinding of capping proteins to filament ends (22). In addition, Zhuravlev and Papoian found that capping proteins induce bundle thinning, leading to the eventual full collapse of filopodia, suggesting a microscopic mechanism for filopodial aging and limits on their lifetime (22).

Excluded volume effects have been studied in the context of macromolecular crowding in cells. It has been shown that crowding introduces a size-dependent viscosity inside the cytoplasm (29), rendering the motion of proteins highly non-trivial. The complex structure of chromatin inside cell nuclei leads to a significant reduction of the effective diffusion coefficient of fluorescent probes (30) thereby possibly influencing and regulating the transcription of DNA into mRNA and the subsequent translation into proteins. Simulation studies and analytical work considering volume exclusion done on chromatin structure extracted from real nuclei via x-ray tomography showed that there exists an optimal amount of volume exclusion that minimizes the mean time for DNA-binding proteins to find their binding sites (31). Theoretical works have shown that Brownian motion with hard-sphere interactions can be captured via an effective, collective diffusion constant (32). Considerably less work has been done to study the feedback between growing cytoskeletal structures and the resulting restriction of the free diffusion of their building blocks.

Here, we show that excluded volume effects also result in filament collapse and bundle thinning. However, in contrast to the effect of capping protein, steric constraints on G-actin diffusion in the bundle interior result in geometrically preferential growth-retraction patterns. Instead of any filament in a bundle being susceptible to collapse due to capping, core filaments in the bundle are starved of G-actin and eventually collapse. G-actin monomers are proteins with an approximately ellipsoidal shape, with the semi-principal axes of $6.7 \times 4 \times 3.7\,\mathrm{nm}$ (33). In addition, both cytosolic and filamentous actin molecules are negatively charged, resulting in their mutual electrostatic repulsion. Because a typical electrostatic screening length is on the order of 1 nm under physiological conditions (34), the electrostatic repulsion is expected to add approximately 2 nm to the steric exclusion zone (35) when considering penetration of G-actin molecules in-between two F-actin filaments. In our calculations, we consider G-actin as spherical particles with a radius of $3.5\,\mathrm{nm}$, averaging over its ellipsoidal semi-axes and also taking into account the screened electrostatic repulsion between G-actin and F-actin. The diameter of actin filaments is approximately $7\,\mathrm{nm}$ (36–38). The average inter-filament spacing inside a bundle of actin filaments is $12\,\mathrm{nm}$ (39–41) with a range of about $10 - 13\,\mathrm{nm}$ (41). In terms of lateral geometrical placements, actin filaments in a filopodial bundle were found to be arranged on an ordered hexagonal lattice (39). Therefore, the geometry of the porous networks found in these tightly cross-linked bundles is likely to impede monomeric G-actin passing through the space between two neighboring filaments. The resulting hindered

diffusion of G-actin restricts availability of G-actin in the bundle interior.

Our simulations show that the above outlined steric exclusion has profound effects on the shape of the filopodial tip. The initial transient growth phase, during which some interior filaments collapse, results in a stationary filament length configuration that is only meta-stable. Over time, interior filament height fluctuations drive them below a mean-field cut-off height (discussed below), when they subsequently collapse to a new meta-stable configuration at an intermediate height and eventually collapse completely. The partial or full collapse of an interior filament creates a new diffusion channel for G-actin to explore. These channels determine the subsequent critical lengths for the fluctuations of the remaining interior filaments. Hence, the further evolution of the inner filament heights is highly dependent on the time ordering of previous filament collapses, leading to history-dependent meta-stable filopodial states. Over time, these processes completely hollow out the interior of actin bundle at the filopodial top, while leaving the peripheral filaments largely intact. In terms of long-term evolution, such a hollow structure may not be stable with respect to the activity of cross-linking and motor proteins, leading to a global geometric reshaping of the filopodial actin bundle, which, in turn, would significantly diminish its mechanical stability, as discussed below.

In the next section, we discuss our methodology and tools. In Section 3, we present our simulation results and discuss the most salient meta-stable states arising from the volume exclusion effects. In Section 4, we introduce a mean-field model that allows us to gain further insight into the stability conditions of the observed states, finding that the mean-field predictions for the heights of partially collapsed filaments closely agree with the Brownian dynamics simulation results. Finally, we analyze the mechanical implications of the morphological transitions induced by the above-mentioned excluded volume effects.

2 MATERIALS AND METHODS

In order to investigate how steric interactions among filaments and G-actin monomers affect actin polymerization dynamics, we have developed a simulation model that incorporates excluded volume effects. In our model, we allow the elongation of actin filaments via binding of G-actin molecules. G-actin particles are allowed to move according to Brownian Dynamics (BD, see below) and can bind to microfilaments when they enter the vicinity of a binding site on top of a filament, thereby elongating the filament by a length δ. Note that the real mechanism of actin polymerization at the filopodial tip may be more complicated and involves additional protein complexes such as ENA/VASP and formins. Therefore our model should be treated as effectively averaging over these details with an effective (or renormalized) polymerization rate. The simulation model proceeds via discrete time steps $\Delta t = 100\,\text{ns}$, in which molecules first move via the BD step, subsequently molecules near binding sites are allowed to bind, and finally G-actin can depolymerize from the tips of filaments, freeing a molecule and reducing the filament length by δ. The parameter values used in this study are summarized in Table 1. We ran 200 distinct realizations of this model for 2,000 seconds each to extract filament height trajectories over time for three different values of the interfilament spacings (taking approximately 50,000 CPU hours).

Table 1: Parameter values used throughout this study. The numbers in the third column indicate references for the cited parameter values.

Description	Value	Ref.
G-actin parameters		
Diffusion constant	$D = 5\times10^6\,\text{nm}^2\,\text{s}^{-1}$	(13)
Bulk G-actin	$c_0 = 10\,\mu\text{M}$	(42)
Geometry		
Filopodial radius	$R = 75\,\text{nm}$	(11)
Filament spacing	$d = 11, 12, 13\,\text{nm}$	(39–41)
Filament radius	$r_F = 3.5\,\text{nm}$	(36–38)
Filament number	$N = 19$	(12)
Filament dynamics		
Binding radius	$\varrho = 2r_F$	
Actin on rate	$k^+ = 11.6\,\mu\text{M}^{-1}\,\text{s}^{-1}$	(43, 44)
Actin off rate	$k^- = 1.4\,\text{s}^{-1}$	(43, 44)
Retrograde flow	$v = 70\,\text{nm}\,\text{s}^{-1}$	(21)
Polymer. length	$\delta = 2.7\,\text{nm}$	(21)
Membrane interaction		
Membrane force	$f = 10\,\text{pN}$	(21, 45)
Fluctuation size	$\sigma = 20\,\text{nm}$	(21, 45)
Temperature	$k_BT = 4.1\,\text{pN nm}$	(13)

2.1 Particle-based stochastic model for diffusion

Our spatially-extended stochastic model for filopodial growth is confined to a spatial domain with cylindrical shape of variable length $L(t) = L_F(t) + 25\,\text{nm}$ (depending on the length of the filopodium at a time t, which is given by the highest filament at the $L_F(t)$) and radius $R = 75\,\text{nm}$. G-actin monomers can enter and exit the domain via the boundary at the bottom, which is held at a constant concentration. These particles undergo BD with a fixed time step Δt, i.e. their position is updated according to $\mathbf{X}_j(t+\Delta t) = \mathbf{X}_j(t) + \sqrt{2D\Delta t}\,\boldsymbol{\xi}_j$ with $j = 1, 2, \ldots, N_A(t)$, where $N_A(t)$ is the number of G-actin molecules at a given time t, and $\boldsymbol{\xi}_j$ is a vector of independent normally distributed random numbers with zero mean and unit variance. Volume exclusion of filaments and boundaries are handled via reflection along the surface normal.

2.2 Volume exclusion

Filaments are modeled as rigid cylinders with a finite radius r_F placed in a hexagonal arrangement (see Section 2.6). To account for the spatial extent of G-actin molecules (which is assumed to be spherical, with the same radius r_F), the effective radius of filaments is given as $2r_F$ (and diffusing molecules are implemented as points). To facilitate this study, G-actin molecules do not mutually interact, hence we do not take queuing and crowding effects into account as this would become computationally prohibitive. The concentration of G-actin is relatively small, hence we do not expect large effects from neglected interactions of G-actin molecules.

2.3 Molecule binding

In order to model the binding of molecules to filament tips, we implement a reversible binding scheme (46), with a binding radius of $\varrho = 2r_F = 7\,\text{nm}$. In this scheme, molecules become binding candidates as soon as they enter a sphere of radius ϱ around the tip of a filament. They are then allowed to bind to the site with a probability P_λ per time step that they spend in the binding region (46, 47). In the vicinity of the top of the filopodium, the binding probability is modified to take the force enacted on the bundle via the membrane into account (see below). We calculate the remaining parameter P_λ (binding probability) before the start of simulations using the approach described in (46, Section 5). To implement depolymerization, a molecule is allowed to dissociate from a filament tip with a probability $1 - \exp(-k^- \Delta t)$ and placed at the former position of the tip. Here, we neglect possible changes in the depolymerization rate due to the hydrolysis of actin molecules as the resulting large fluctuations in filament length occur only at actin concentrations much smaller than exist in our simulations (48).

2.4 Membrane force

Experiments have shown that the actin polymerization rate highly depends on the force enacted on filaments by the membrane (49). This effect can be thought of as temporary envelopment of a filament tip by the membrane, sterically disallowing the binding of G-actin to the tip, thereby synchronizing the movement of the filament tips close to the membrane (21). Thus, the bare bulk polymerization rate k^+ needs to be multiplied by the probability for the creation of enough space between a filament tip and the membrane to accommodate the molecule. This Brownian ratchet model allows us to take into account membrane effects without explicitly simulating the movement of the membrane by modifying the binding probability of G-actin molecules inside the binding radius of the i-th filament (22, 45)

$$P_\lambda^{(i)} = P_\lambda \exp\left(-\frac{f_i \delta}{k_B T}\right), \qquad i = 1, 2, ..., N, \qquad (1)$$

where f_i is the force on filament i. On the micrometer scale, the cell membrane is known to equilibrate on the order of microseconds (50), hence much faster than the average time between polymerization reactions. Therefore, f_i is proportional to the probability of the filament tip being covered by the membrane. Assuming Gaussian-distributed membrane height fluctuations, we can follow Lan and Papoian (21) to calculate the probability of the membrane being below the filament tip

$$p_i = \frac{1}{2}\text{erfc}\left(\frac{\max\{h_j\} - h_i}{\sigma}\right),$$

where $\text{erfc}(x) = 1 - \text{erf}(x)$ is the complementary error function and h_j is the height of the j-th filament. The total membrane force f is distributed across all the filaments according to this probability, hence the force on filament i is

$$f_i = \frac{p_i f}{\sum_{j=1}^{N} p_j},$$

which we can substitute into Eq. (1) to get the effective polymerization probability.

Wang and Carlsson (51) model the motion of a Brownian obstacle (the membrane in our case) pushed by polymerizing filaments. They disallow polymerization when the distance to the membrane is less than the monomer size and let polymerization proceed with the bare rate k^+ otherwise. Das *et al.* (52) consider a discrete lattice model for filament polymerization against an external load that reduces the polymerization rate of the leading filament (in contact with the obstacle) only. Our model differs from both of these in that we assume a non-rigid, highly dynamic membrane as the obstacle, which can affect the polymerization of filaments even a distance below the mean membrane position (21).

2.5 Filament polymerization and collapse

The dynamics of actin filaments are governed by the inherent asymmetry between the two ends of a filament. The barbed end (the filament tip in our simulations) exhibits a much higher polymerization rate, which leads to a treadmilling process. Actin microfilaments grow via the binding of G-actin monomers, which enhances the filament length by $\delta = 2.7\,\text{nm}$. The binding algorithm implemented in our simulations is discussed above. The bulk polymerization rate is given by $k_A^+ = 11.6\,\mu\text{M}^{-1}\,\text{s}^{-1}$ from which we calculate the binding probability for a given binding radius. The binding radius cannot be larger than half of the distance between filaments such that the binding region does not overlap with excluded volume regions, thereby artificially lowering the

effective binding rate. During a depolymerization reaction, the filament's height is reduced by a length δ and a new G-actin molecule is placed at the former position of the filament tip. Enhanced depolymerization processes at the spiked ends of actin filaments in the lammellipodium lead to a pulling back motion of filaments called retrograde flow. We incorporate this in our simulation model via a constant and negative effective velocity of filament tips v. During each time step, each filament's height shrinks by $v\Delta t$, in addition to any depolymerization reaction occurring during this time step.

2.6 *Lateral position of filaments and initial state*

Filaments are placed in a hexagonal arrangement with an initial height of 100 nm. The in-plane coordinates $\vec{x}_i$ of the $N = 19$ filaments are given by

$$(0,0),\quad (0,d),\quad (\sqrt{3}d/2, d/2),\quad (\sqrt{3}d/2, -d/2),$$
$$(0,-d),\quad (-\sqrt{3}d/2, -d/2),\quad (-\sqrt{3}d/2, d/2),$$
$$(\sqrt{3}d/2, 3d/2),\quad (\sqrt{3}d, 0),\quad (\sqrt{3}d/2, -3d/2),$$
$$(-\sqrt{3}d/2, -3d/2),\quad (-\sqrt{3}d, 0),\quad (-\sqrt{3}d/2, 3d/2),$$
$$(0, 2d),\quad (\sqrt{3}d, d),\quad (\sqrt{3}d, -d),\quad (0, -2d),$$
$$(-\sqrt{3}d, -d),\quad (-\sqrt{3}d, d),$$

with d the next-neighbor distance. The hexagonal arrangement of microfilaments in a bundle has been observed in experiments (39) and is close to an optimal cross-sectional configuration for a bundle of actin filaments, maximizing an individual filament's number of next neighbors.

3 RESULTS

When filopodial growth dynamics are simulated using the approach described above, we find that, typically, an actin filament bundle undergoes several transitions between meta-stable configurations. Initially, a rapid growth phase is observed, during which all filaments grow together, followed by intermittent collapses of filaments *inside* the bundle. Hence, the bundle settles into different meta-stable steady states, during which the filament heights fluctuate around particular quasi-stationary values. These quasi-stationary heights are determined by a balance between the polymerization of G-actin and the combination of depolymerization of F-actin and retrograde flow (see Section 4) (21, 53). At intermediate times, large fluctuations of single filaments push the bundle out of the current meta-stable state and one or more filaments further collapse. This collapse can be complete (a filament's height shrinks to zero and it disappears) or partial. In the case of a partial collapse, collapsed filaments fluctuate around a new, lower height, which is largely determined by a changed supply of G-actin molecules due to the new bundle geometry. Hence, the bundle height transitions due to individual filament collapses are exclusively driven by the fluctuations of G-actin's availability mediated by local steric constraints. This is in contrast to filament collapse due to the binding of capping proteins that instead directly halt filaments' polymerization propensities (22). Note that the polymerization reaction is always diffusion limited, because the filaments will simply grow until a balance is reached between the addition of new monomers and the reduction in length due to depolymerization and retrograde flow (21). Hence, our results are robust even for greater G-actin concentrations or large uncertainties in the polymerization rate parameter. We checked this with sets of simulations with $c_0 = 20\,\mu\text{M}$, $k^+ = 5\,\mu\text{M}^{-1}\,\text{s}^{-1}$ and $k^+ = 20\,\mu\text{M}^{-1}\,\text{s}^{-1}$ (see below).

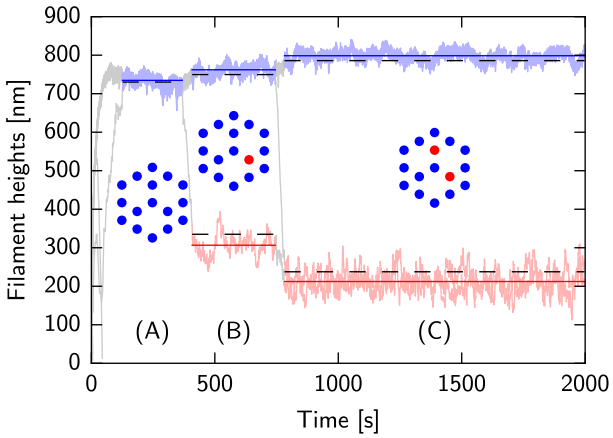

Figure 2: *Filament heights over time from a representative simulation run with* $d = 13\,\text{nm}$. *The upper filament trajectories at the bundle tip are highlighted in blue, the partially-collapsed filament trajectories are shown in red. All filaments are accounted for in these two categories during an identified meta-stable state. Three distinct meta-stable states are visible in order of appearance in the graph:* (A) *Three completely collapsed filaments with the remainder at the tip of the bundle;* (B) *one of the inner filaments collapsed partway;* (C) *two inner filaments collapsed partway. The insets show the spatial configuration of the meta-stable states. The black dashed lines indicate the filament heights calculated from Eq.* (6). *Gray lines indicate transient states between meta-stable configurations.*

Fig. 2 shows filament height dynamics from a representative simulation run. The height data clearly reveal three distinct meta-stable states, which were automatically identified using the DBSCAN clustering algorithm (54, 55). Uncategorized data are shown as light gray lines, while colored line plots show filament height data belonging to an identified meta-stable configuration. The insets show a top view of the spatial distribution of filaments inside the bundle. Blue circles indicate the lateral positions of filaments in the cluster at the filopodial top; red circles are the positions of filaments

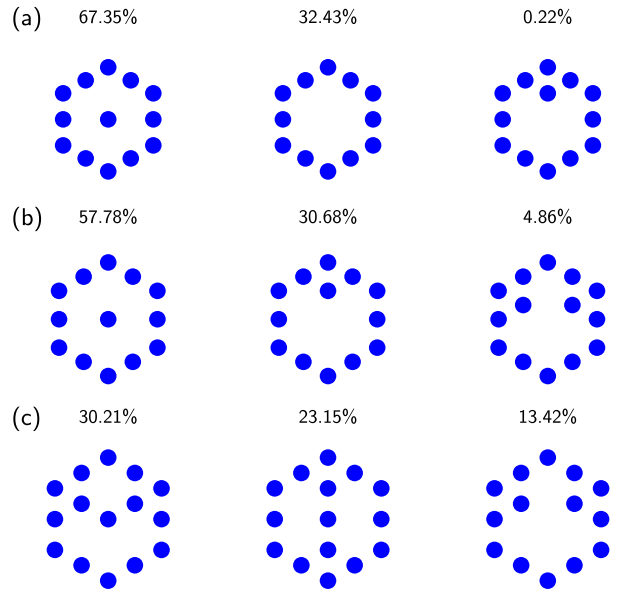

Figure 3: *The spatial distribution of full-length filaments in the actin filament bundle inside the filopodium, displayed for the* 3 *most prevalent configurations out of* 16 *found for* (a) $d = 11$ nm, (b) $d = 12$ nm *and* (c) $d = 13$ nm. *A blue color indicates full-length filaments, while white space indicates partially or fully collapsed filaments. The numbers above the individual states indicate the percentage of total simulation time spent in this state.*

that are part of an intermediate-height cluster; and white spaces indicate the former positions of filaments that collapsed completely. Importantly, these empty spaces serve as additional channels for G-actin to diffuse inside the bundle.

After the brief initial transient, Fig. 2 shows that three filaments have completely collapsed and disappeared. The resulting bundle is found, therefore, in a highly symmetric configuration with all remaining filament tips at the top of the filopodium. Subsequently, at $t \approx 400$ s, a large fluctuation drives a single filament tip below the stable region and it collapses towards a level of about 300 nm. Note that at the same time, the filopodial tip (i.e. the filament cluster at the tip of the filopodium) grows slightly. At the second transition point, at $t \approx 750$ s, a second filament collapses partway and joins the lower cluster. The two filament's height shrinks slightly while the filopodial tip grows again. The occurrence of these meta-stable states, together with the transitions between them strongly indicates the existence of multi-stability in this system. When filament tips inside the bundle leave the region of attraction of a stable cluster, they collapse partway and reach a different meta-stable state.

Over time, this leads to a hollowing out of the filament bundle, which, in turn, has interesting implications for the mechanical and geometrical properties of the filopodium.

Fig. 3 shows the three most prevalent meta-stable configurations (considering only the filaments that are positioned at the top of the bundle), ranked by the percentage of time spent in this state throughout our study (we accounted for symmetries that make configurations equivalent) for a filament spacing of $d = 11, 12$ and 13 nm (as this covers the majority of interfilament distances observed in experiments (41)). Blue circles represent filaments that reach the top of the filopodium, while white spaces indicate completely or partially collapsed filaments (i.e. open diffusion channels inside the bundle). All of these configurations show a thinning of the filament bundle towards the filopodial top. As a general rule, when filaments in the bundle are positioned with smaller interfilament spacings with respect to each other, the inner filaments are more likely to collapse.

Because the parameter values listed in Table 1 might have large associated uncertainties or might apply only to a limited range of cell types, we tested whether our observed effects are present also for different parameter values. We systematically varied the following parameters:

- **Bulk G-actin concentration:** The reported G-actin concentration measured in various cell types and organisms ranges between 10 to 100 µM and sometimes even higher (42, 56). However, for the purposes of our simulation study it is crucially important to distinguish not only between monomeric G-actin and polymerized F-actin, but also between G-actin that is available to polymerize and sequestered G-actin (i.e. bound to other proteins such as cofilin or thymosin-$\beta 4$). The latter is unavailable to directly polymerize into filaments und therefore needs to be excluded. From quantitative simulation studies, Mogilner and Edelstein-Keshet (57) estimate the available unsequestered G-actin in the lamellipodium to be $\approx 14\,\mu$M when the total available actin concentration was $250\,\mu$M. From this, Zhuravlev *et al.* estimate a valid unsequestered G-actin concentration ranging between $1 - 50\,\mu$M (56, Supporting table 1).

  To check if our results are valid for higher concentrations within this range, we ran simulations for $c_0 = 20\,\mu$M, leading to a roughly doubled length of the filopodium in which the collapse of inner filaments together with meta-stable states still occur. We do not expect this to change for even higher G-actin concentrations, because inner filaments are always at a disadvantage due to the lower supply of G-actin monomers as long as bundles are able to grow when polymerization of filaments outperforms depolymerization and retrograde flow:

  $$c_0 k^+ > k^- + v_{ret}/\delta \approx 27.6\,\mathrm{s}^{-1}\,.$$

  For $k^+ = 11.6\,\mu\mathrm{M}^{-1}\,\mathrm{s}^{-1}$, this is the case when $c_0 > 2.4\,\mu$M. Due to possibly large exchange rates between sequestered and unsequestered G-actin (58) the bulk G-actin concentration might be higher than assumed (and

therefore the effective polymerization rate lower than measured). However, our arguments above show that our results are valid even then.

- **G-actin polymerization rate:** We ran additional simulations with a polymerization rate of $k^+ = 5\,\mu\text{M}^{-1}\,\text{s}^{-1}$ and $k^+ = 20\,\mu\text{M}^{-1}\,\text{s}^{-1}$. In the latter case, the length of the filopodium is enhanced, but the reported effects due to steric interactions are still observable. The filopodia become very short ($< 300\,\text{nm}$) in the former case, and the probability of partially collapsed filaments recovering (instead of collapsing completely) to the filopodial tip becomes significantly higher, which is to be expected because small positive height fluctuations are then sufficient to reach the upper stable configuration. We also ran simulations with a doubled G-actin concentration $c_0 = 20\,\mu\text{M}$ and an approximately halved G-actin polymerization rate of $k^+ = 5\,\mu\text{M}^{-1}\,\text{s}^{-1}$, yielding filopodia of a length of about $1.4\,\mu\text{m}$ with hollow bundles.

- **Diffusion constant:** To check the influence of the diffusion constant, we ran simulations with $D = 2.5 \times 10^6\,\text{nm}^2\,\text{s}^{-1}$. This also led to a significantly reduced filament height (which is to be expected), similar to the reduction in the polymerization rate.

Therefore we conclude that our observed actin bundle remodeling effects are indeed robust against relatively large changes in the G-actin parameter values.

In an earlier work, Mogilner and Rubinstein (13) analyzed the mechanical stability of a filopodial bundle. At the maximum stable length, L, the force enacted on the bundle via the membrane F is equal to the buckling force of the bundle (59)

$$F = \frac{\pi^2 B_s}{4L^2}\,, \tag{2}$$

where $B_s = EI$ is the bending stiffness, E is Young's modulus and I the second moment of area (interactions with filament cross-linking molecules are not considered). The resulting buckling length is $L = \pi\sqrt{B_s/4F}$. When considering single actin filaments in the bundle as filled rods, the bending force and hence the buckling length of different lateral arrangements of filaments differ only in their second moment of area. A single filament with radius r_F, cross-sectional area A and distance $\vec{a}$ from the bundle center contributes to the bundle's second moment of area via the Huygens-Steiner theorem

$$I_s(a) = \int_A |\vec{r} - \vec{a}|^2 dA = \frac{\pi}{4} r_F^4 + \pi r_F^2 a^2\,.$$

Hence, a full bundle in an hexagonal arrangement with inter-filament spacing d with 19 filaments has a second moment of area of

$$\begin{aligned} I_F &= I_s(0) + 6I_s(d) + 6I_s(2d) + 6I_s\big(\sqrt{3}d\big) \\ &= \pi r_F^2 \left(\frac{19}{4} r_F^2 + 48 d^2\right)\,. \end{aligned}$$

A hollow bundle in an hexagonal arrangement with all seven inner filaments collapsed exhibits a second moment of area of

$$I_O = 6I_s(2d) + 6I_s\big(\sqrt{3}d\big) = \pi r_F^2 \big(3r_F^2 + 42d^2\big)\,.$$

Hence, the buckling length ratio between hollow and intact filopodial bundles is (assuming $d = 13\,\text{nm}$)

$$f = \sqrt{\frac{3r_F^2 + 42d^2}{\frac{19}{4} r_F^2 + 48 d^2}} \approx 0.93\,.$$

Therefore, the maximum stable length of a totally hollowed-out bundle is reduced to 93% of the intact bundle, i.e. the effect on the mechanical stability is rather weak. If, on the other hand, the bundle is laterally coalesced into a hexagonal arrangement by, for example, strong cross-linker interactions or molecular motors, the second moment of area becomes

$$I_C = I_s(0) + 6I_s(d) + 5I_s\big(\sqrt{3}d\big) = \pi r_F^2 \big(3r_F^2 + 21d^2\big)\,,$$

and the above-mentioned length ratio becomes $f \approx 0.66$, producing a much larger effect because of the reduced cross-sectional area of the filament bundle.

4 MEAN-FIELD MODEL

In order to provide deeper understanding into the processes that lead to filament collapse inside the bundle's core, we next introduce the following simplified model. We assume that G-actin diffusion occurs fast, such that linear concentration profiles are quickly established along the filopodia axis. The arrangement of filaments is such that G-actin cannot pass between two neighboring filaments. Fig. 4(a) shows a sketch of this channel configuration. Hence, there exist at least two separate channels for diffusion in the filopodium: G-actin can diffuse along and *outside* of the filament bundle, as well as via any inner space that opens up due to filament collapse. This inner channel can then host filaments that are partially collapsed, which yields a changing cross-sectional area of the diffusion channel. The outer channel exhibits a cross-sectional area A_1. The area of the inner lower channel is given by A_2, which widens to A_3 at the partially-collapsed filaments tip position L_1. The two channels merge to a single diffusion channel with area $A_4 = \pi r_F^2$ at the bundle's tip L_2. In a meta-stable state, the filament tips in the partially-collapsed level as well as the bundle's top both consume just enough G-actin in order to hold their height stable. The G-actin concentrations in the corresponding channels c_1, c_2, c_3

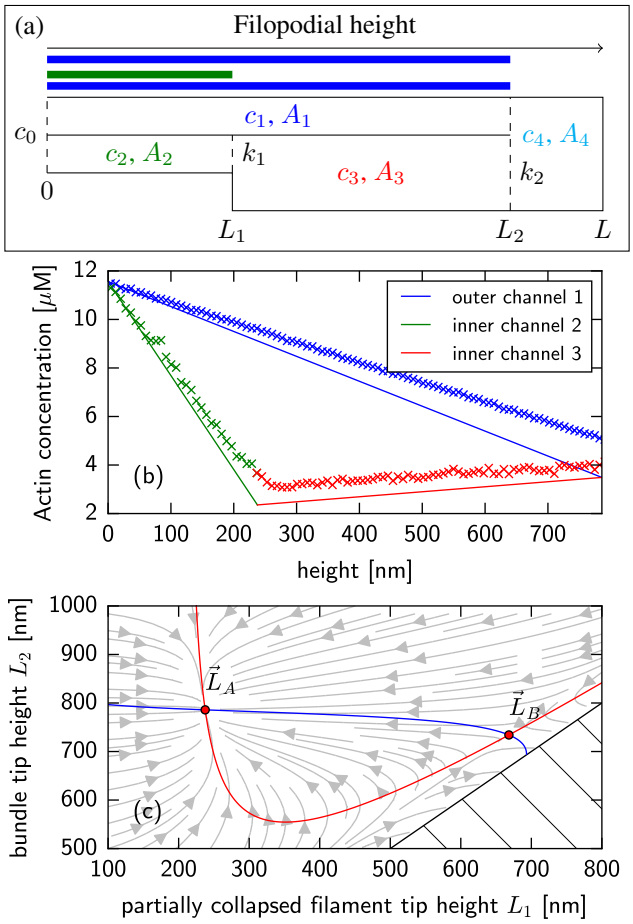

Figure 4: (a) *Sketch of the one-dimensional diffusion channels considered as part of the mean-field model for a filopodium with two distinct filament heights. The two channels exhibit x-dependent piece-wise linear concentrations c_1, c_2, c_3 and c_4. The lower channel changes its cross-section at position L_1 due to the presence of one or more filament tips. At position L_2, both channels merge and the cross-sectional area changes again with $A_1 + A_3 < A_4$. The membrane is at $L = L_2 + 25\,\text{nm}$. Polymerization of G-actin is implemented via sinks with strength k_1 and k_2 at positions L_1 and L_2, respectively.* (b) *Mean-field G-actin concentration profiles in the three channels for meta-stable configuration* (C) *displayed in Fig.* 2 *together with data from stochastic simulations.* (c) *Plot of the roots of the two stability conditions* (6) *as a function of L_1 and L_2 for the same configuration. The points of filament stability where both conditions are true simultaneously are indicated by red dots. The light gray lines show the flow of the stability conditions* (6)*. The hatched area indicates the unphysical regime $L_1 \geq L_2$.*

Table 2: Membrane factor values obtained from simulations.

N_2	$f_M(N_2)$	N_2	$f_M(N_2)$
12	0.779	16	0.823
13	0.792	17	0.831
14	0.804	18	0.838
15	0.814	19	0.845

and c_4 then follow the set of diffusion equations

$$\begin{aligned} \frac{d^2c_1}{dx^2} &= 0,\ x \in [0, L_2] \qquad \frac{d^2c_2}{dx^2} = 0,\ x \in [0, L_1] \\ \frac{d^2c_3}{dx^2} &= 0,\ x \in [L_1, L_2] \qquad \frac{d^2c_4}{dx^2} = 0,\ x \in [L_2, L]\ , \end{aligned} \tag{3}$$

with the conditions at the boundaries of the different channels

$$\begin{aligned} c_1(0) &= c_2(0) = c_0\ , \\ c_2(L_1) &= c_3(L_1)\ , \\ c_1(L_2) &= c_3(L_2) = c_4(L_2)\ , \end{aligned} \tag{4}$$

and the flux conditions across these boundaries

$$\begin{aligned} A_2\frac{dc_2}{dx}(L_1) - A_3\frac{dc_3}{dx}(L_1) &= -\frac{k_1}{D}c_3(L_1)\ , \\ A_1\frac{dc_1}{dx}(L_2) + A_3\frac{dc_3}{dx}(L_2) &= -\frac{k_2}{D}c_4(L_2)\ , \\ \frac{dc_4}{dx}(L) &= 0\ . \end{aligned} \tag{5}$$

The coefficient of the reactive boundary condition describing the removal of G-actin by the N_1 partially-collapsed filament tips is given by $k_1 = N_1 k^+/N_A$, where N_A is Avogadro's constant. Similarly, the removal of molecules via the N_2 filaments at the bundle tip is implemented by a reactive boundary condition at L_2 with the coefficient $k_2 = f_m(N_2)N_2k^+/N_A$. The factor $f_m(N_2)$ stems from the steric interactions of G-actin with the membrane at the top of the filopodium, and is calculated via

$$f_m(N_2) = 0.550 + 2.524 \times 10^{-2}N_2 - 5.131 \times 10^{-4}N_2^2\ ,$$

where the coefficients result from a fit of a polynomial of order 2 to data generated in simulations and listed in Table 2. Eqs (3)-(5) can be written as a system of linear equations for the concentrations at the filament tips $c_3(L_1)$ and $c_1(L_2)$.

Fig. 4(b) shows the resulting linear concentration profiles in the respective channels for the example configuration (C) shown in Fig. 2, together with data obtained from our simulations. As discussed above, filament heights are (meta-)stable when the polymerization of G-actin with rate k^+ is counterbalanced by the effective reduction in length due to the depolymerization reaction with rate k^- and retrograde flow with speed v. Thus, the stability criteria are given by

$$f_m\, k^+ c_1(L_2)\frac{A_1}{A_4} = k^- + \frac{v}{\delta}\ , \quad k^+c_3(L_1) = k^- + \frac{v}{\delta}\ , \tag{6}$$

where $c_1(L_2)$ and $c_3(L_1)$ are the concentrations of G-actin at the filament tip positions L_2 and L_1 in channels 1 and 3, respectively. The area ratio is necessary due to the geometry of the bundle. The effective reduction of the polymerization rate at the L_2 tip position due to membrane interaction is taken into account by the phenomenological factor f_m. These criteria together with the solution from Eqs. (4)-(6) describe two non-linear curves in the $0 < L_1 < L_2$ sector of the plane spanned by L_1 and L_2. If there exists a stable configuration, the two curves intersect in two points, which are given by $\vec{L}_A = (L_{1,A}, L_{2,A})$ and $\vec{L}_B = (L_{1,B}, L_{2,B})$. The point $\vec{L}_A$ is a stable configuration within the limits of this model, while the point $\vec{L}_B$ is a saddle point that mediates the collapse of filaments from the bundle tip. Fig. 4(c) shows the two curves and their intersection points for configuration (C) shown in Fig. 2. The light gray arrows indicate the vector field

$$\left(\frac{f_m k^+ c_1(L_2)}{k^- + v/\delta} \frac{A_1}{A_4} - 1, \frac{k^+ c_3(L_1)}{k^- + v/\delta} - 1 \right),$$

which corresponds to the flow of the filament stability conditions (6). In the stochastic simulation model, the point $\vec{L}_B$ becomes quasi-stable. As soon as a fluctuation in the height of a single filament causes it to fall approximately 100 nm below $L_{1,B}$, the single filament will collapse to the height $L_{1,A}$ and the bundle tip will move to a length $L_{2,A}$.

The black dashed lines in Fig. 2 show the predicted filament heights for three different meta-stable configurations, with very good agreement with our simulation data. The observed overestimation of the height of the partially collapsed filaments and the underestimation of the height of the bundle tip stems from the inability of the theory to capture the more complicated spatial structure inside a bundle. This is also the reason for the discrepancy between the mean field concentrations and the data from stochastic simulations in Fig. 4(b).

In order to find the parameter regimes in which meta-stable bundle configurations exist (rather than inner filaments simply collapsing completely), we extracted the mean-field stability boundary of the bundle configuration (C) in Fig. 2 in the manuscript via finding the value of $k^+(c_0)$ at which Eqs. (6) start to have solutions. It is well described by the curve given as $c_0 k^+ \approx 63.8\,\mathrm{s}^{-1}$. However, this only applies to this particular bundle configuration. When we repeat the same analysis over all bundle configurations we observe in simulations with $D = 5 \times 10^6\,\mathrm{nm}^2\,\mathrm{s}^{-1}$ and $d = 13\,\mathrm{nm}$ but varying c_0 and k^+, the minimum value is $\alpha = c_0 k^+ \approx 46.9\,\mathrm{s}^{-1}$. This value of α can be viewed as the upper limit for the phase boundary between immediate collapse of inner filaments ($c_0 k^+ < \alpha$) and the existence of meta-stable filament heights ($c_0 k^+ > \alpha$).

5 DISCUSSION

Our results show that the sterically hindered movement of free G-actin molecules leads to intriguing effects: When G-actin cannot pass between filaments in the filopodial shaft bundle, the polymerization of barbed ends of F-actin inside the bundle may not be sufficient to counteract retrograde flow. However, instead of the complete collapse of all filaments, novel meta-stable intermediate-height states emerge. Interior filaments that arise from an initial transient growth regime, initially have similar heights compared with the stable exterior filaments. However, height fluctuations will eventually drive single or multiple interior filaments below a critical stable height $L_{1,B}$, after which they collapse to a new meta-stable height $L_{1,A}$. We verified that this effect is present for different values of the interfilament spacing d observed in experimental measurements of actin bundles. Our mean-field model enables us to approximately calculate the expected critical heights for a given configuration. As these new states are only meta-stable, the partially collapsed filaments will eventually collapse fully and disappear. This, in turn, opens up new diffusion channels for G-actin molecules, raising their concentration in the bundle interior and thereby enhancing the stability of any remaining interior filaments. Due to the raised supply of G-actin, the average height of the topmost filament tips is raised as well.

The configuration of the filament bundle at any given time depends on the history of all prior filament collapses starting from the initial transient. Therefore, the ensemble of observed bundle configurations is highly diverse, with a small selection of configurations shown in Fig. 3. Over time, the interior of the bundle becomes hollowed-out with some interior filaments collapsing partially or completely. Thus, volume exclusion and the resulting change in the free diffusion of G-actin facilitates sculpting of the actin bundle inside filopodia. This reaction-diffusion sculpting mechanism adds complexity to the formin/capping protein mediated filament dynamics investigated in reference (22).

Furthermore, we should consider the possibility that internal forces due to filament cross-linking proteins or molecular motors may laterally constrict bundles with collapsed internal filaments. Hence, as the filopodium ages, two outcomes are likely: 1) After the bundle becomes hollowed-out due to reaction-diffusion sculpting, it continues to remain hollow (for example, because of weak cross-linking activity), experiencing only a small reduction of its initial mechanical stability, as discussed above; 2) The bundle shrinks radially due to inward internal forces collapsing the hollow cavity, which, in turn, would lead to a strong reduction of bundle's mechanical stability. This second scenario would imply an overall conical shape of aged filopodial bundles, with a thicker portion position near the filopodial base and a thinner section positioned at the filopodial tips, hence, explaining the corresponding common observations

of conically shaped actin filament bundles in superresolution and fluorescence microscopy imaging of filopodia; see e.g. figure 1A in reference (60) or figure 1C in reference (61). Tapering of long filopodial protrusions has also been reported in sea urchins (62), in epithelial cells (63) and in plant cells (64).

AUTHOR CONTRIBUTIONS

U.D. wrote and performed the simulations; U.D. and R.E. evaluated the computed results; U.D., G.A.P. and R.E. designed the project and co-wrote the paper.

ACKNOWLEDGMENTS

The research leading to these results has received funding from the European Research Council under the European Community's Seventh Framework Programme (FP7/2007-2013) / ERC grant agreement n^o 239870. R.E. would like to thank the Royal Society for a University Research Fellowship and the Leverhulme Trust for a Philip Leverhulme Prize. This prize money was used to support research visits of G.A.P. in Oxford. His work was also supported by NSF grant CHE-1363081. R.E. and U.D. would like to thank the Isaac Newton Institute for Mathematical Sciences, Cambridge, for support and hospitality during the programme "Stochastic Dynamical Systems in Biology: Numerical Methods and Applications" where work on this paper was undertaken. This work was supported by EPSRC grant no EP/K032208/1. This work was partially supported by a grant from the Simons Foundation. U.D. was supported by a Junior Interdisciplinary Fellowship via Wellcome Trust grant number 105602/Z/14/Z.

References

1. Mattila, P. K., and P. Lappalainen, 2008. Filopodia: molecular architecture and cellular functions. Nat. Rev. Mol. Cell Biol. 9:446–454.
2. Small, J., and K. Rottner, 2010. Elementary Cellular Processes Driven by Actin Assembly: Lamellipodia and Filopodia. In M.-F. Carlier, editor, Actin-based Motil., Springer, New York, NY, 3–33.
3. Han, Y.-H., 2002. Requirement of a Vasodilator-stimulated Phosphoprotein Family Member for Cell Adhesion, the Formation of Filopodia, and Chemotaxis in Dictyostelium. J. Biol. Chem. 277:49877–49887.
4. Dent, E. W., and F. B. Gertler, 2003. Cytoskeletal Dynamics and Transport in Growth Cone Motility and Axon Guidance. Neuron 40:209–227.
5. Maletic-Savatic, M., 1999. Rapid Dendritic Morphogenesis in CA1 Hippocampal Dendrites Induced by Synaptic Activity. Science (80-.). 283:1923–1927.
6. Wood, W., A. Jacinto, R. Grose, S. Woolner, J. Gale, C. Wilson, and P. Martin, 2002. Wound healing recapitulates morphogenesis in Drosophila embryos. Nat. Cell Biol. 4:907–912.
7. Arjonen, A., R. Kaukonen, and J. Ivaska, 2011. Filopodia and adhesion in cancer cell motility. Cell Adhes. & Migr. 5:421–430.
8. Sherer, N. M., M. J. Lehmann, L. F. Jimenez-Soto, C. Horensavitz, M. Pypaert, and W. Mothes, 2007. Retroviruses can establish filopodial bridges for efficient cell-to-cell transmission. Nat Cell Biol 9:310–315.
9. Behrmann, E., M. Müller, P. A. Penczek, H. G. Mannherz, D. J. Manstein, and S. Raunser, 2012. Structure of the rigor actin-tropomyosin-myosin complex. Cell 150:327–338.
10. Galkin, V. E., A. Orlova, O. Cherepanova, M.-C. Lebart, and E. H. Egelman, 2008. High-resolution cryo-EM structure of the F-actin-fimbrin/plastin ABD2 complex. Proc. Natl. Acad. Sci. U. S. A. 105:1494–1498.
11. Atilgan, E., D. Wirtz, and S. X. Sun, 2006. Mechanics and dynamics of actin-driven thin membrane protrusions. Biophys. J. 90:65–76.
12. Sheetz, M. P., D. B. Wayne, and A. L. Pearlman, 1992. Extension of filopodia by motor-dependent actin assembly. Cell Motil. Cytoskelet. 22:160–169.
13. Mogilner, A., and B. Rubinstein, 2005. The Physics of Filopodial Protrusion. Biophys. J. 89:782–795.
14. Bray, D., 2001. Cell Movements: From Molecules to Motility. Garland Science, New York, NY.
15. Hotulainen, P., and P. Lappalainen, 2006. Stress fibers are generated by two distinct actin assembly mechanisms in motile cells. J. Cell Biol. 173:383–394.
16. Bear, J. E., T. M. Svitkina, M. Krause, D. a. Schafer, J. J. Loureiro, G. a. Strasser, I. V. Maly, O. Y. Chaga, J. A. Cooper, G. G. Borisy, and F. B. Gertler, 2002. Antagonism between Ena/VASP proteins and actin filament capping regulates fibroblast motility. Cell 109:509–521.
17. Schafer, D. a., P. B. Jennings, and J. A. Cooper, 1996. Dynamics of capping protein and actin assembly in vitro: Uncapping barbed ends by polyphosphoinositides. J. Cell Biol. 135:169–179.
18. Evangelista, M., S. Zigmond, and C. Boone, 2003. Formins: signaling effectors for assembly and polarization of actin filaments. J. Cell Sci. 116:2603–2611.
19. Faix, J., D. Breitsprecher, T. E. B. Stradal, and K. Rottner, 2009. Filopodia: Complex models for simple rods. Int. J. Biochem. Cell Biol. 41:1656–1664.
20. Leijnse, N., L. B. Oddershede, and P. M. Bendix, 2015. An updated look at actin dynamics in filopodia. Cytoskeleton 79:71–79.
21. Lan, Y., and G. A. Papoian, 2008. The Stochastic Dynamics of Filopodial Growth. Biophys. J. 94:3839–3852.
22. Zhuravlev, P. I., and G. A. Papoian, 2009. Molecular noise of capping protein binding induces macroscopic instability in filopodial dynamics. Proc. Natl. Acad. Sci. 106:11570–11575.
23. Mejillano, M. R., S. I. Kojima, D. A. Applewhite, F. B. Gertler, T. M. Svitkina, and G. G. Borisy, 2004. Lamellipodial versus filopodial mode of the actin nanomachinery: Pivotal role of the filament barbed end. Cell 118:363–373.
24. Heid, P. J., J. Geiger, D. Wessels, E. Voss, and D. R. Soll, 2005. Computer-assisted analysis of filopod formation and the role of myosin II heavy chain phosphorylation in Dictyostelium. J. Cell Sci. 118:2225–2237.
25. Mallavarapu, A., and T. Mitchison, 1999. Regulated actin

cytoskeleton assembly at filopodium tips controls their extension and retraction. J. Cell Biol. 146:1097–1106.

26. Aratyn, Y. S., T. E. Schaus, E. W. Taylor, and G. G. Borisy, 2007. Intrinsic dynamic behavior of fascin in filopodia. Mol. Biol. Cell 18:3928–3940.
27. Bornschlögl, T., 2013. How filopodia pull: What we know about the mechanics and dynamics of filopodia. Cytoskeleton 70:590–603.
28. Erban, R., M. B. Flegg, and G. A. Papoian, 2013. Multiscale Stochastic Reaction-Diffusion Modeling: Application to Actin Dynamics in Filopodia. Bull. Math. Biol. 1–20.
29. Kalwarczyk, T., N. Ziebacz, A. Bielejewska, E. Zaboklicka, K. Koynov, J. Szymanski, A. Wilk, A. Patkowski, J. Gapinski, H.-J. Butt, and R. Hoyst, 2011. Comparative Analysis of Viscosity of Complex Liquids and Cytoplasm of Mammalian Cells at the Nanoscale. Nano Lett. 11:2157–2163.
30. Wachsmuth, M., W. Waldeck, and J. Langowski, 2000. Anomalous diffusion of fluorescent probes inside living cell nuclei investigated by spatially-resolved fluorescence correlation spectroscopy. J. Mol. Biol. 298:677–689.
31. Isaacson, S. a., C. a. Larabell, M. a. Le Gros, D. M. McQueen, and C. S. Peskin, 2013. The influence of spatial variation in chromatin density determined by X-ray tomograms on the time to find DNA binding sites. Bull. Math. Biol. 75:2093–2117.
32. Bruna, M., and S. J. Chapman, 2012. Excluded-volume effects in the diffusion of hard spheres. Phys. Rev. E 85:011103.
33. Suck, D., W. Kabsch, and H. G. Mannherz, 1981. Three-dimensional structure of the complex of skeletal muscle actin and bovine pancreatic DNAse I at 6-A resolution. Proc. Natl. Acad. Sci. U. S. A. 78:4319–4323.
34. Spitzer, J., and B. Poolman, 2009. The role of biomacromolecular crowding, ionic strength, and physicochemical gradients in the complexities of life's emergence. Microbiol. Mol. Biol. Rev. 73:371–388.
35. Evans, D. F., and H. Wennerström, 1999. The Colloidal Domain: Where Physics, Biology, and Technology Meet. Wiley-VCH, New York, NY.
36. Tucker, J. B., 1971. Microtubules and a contractile ring of microfilaments associated with a cleavage furrow. J. Cell Sci. 8:557–571.
37. Heath, J. P., and G. a. Dunn, 1978. Cell to substratum contacts of chick fibroblasts and their relation to the microfilament system. A correlated interference-reflexion and high-voltage electron-microscope study. J. Cell Sci. 29:197–212.
38. Fujii, T., A. H. Iwane, T. Yanagida, and K. Namba, 2010. Direct visualization of secondary structures of F-actin by electron cryomicroscopy. Nature 467:724–728.
39. Jasnin, M., S. Asano, E. Gouin, R. Hegerl, J. M. Plitzko, E. Villa, P. Cossart, and W. Baumeister, 2013. Three-dimensional architecture of actin filaments in Listeria monocytogenes comet tails. Proc. Natl. Acad. Sci. U. S. A. 110:20521–6.
40. Urban, E., S. Jacob, M. Nemethova, G. P. Resch, and J. V. Small, 2010. Electron tomography reveals unbranched networks of actin filaments in lamellipodia. Nat. Cell Biol. 12:429–435.
41. Yang, S., F.-k. Huang, J. Huang, S. Chen, J. Jakoncic, A. Leomacias, R. Diaz-avalos, L. Chen, J. J. Zhang, and X.-y. Huang, 2013. Molecular Mechanism of Fascin Function in Filopodial Formation. J. Biol. Chem. 288:274–284.
42. Pollard, T. D., L. Blanchoin, and R. D. Mullins, 2000. Molecular Mechanisms Controlling Actin Filament Dynamics in Nonmuscle Cells. Annu. Rev. Biophys. Biomol. Struct. 29:545–576.
43. Pollard, T., 1986. Rate constants for the reactions of ATP- and ADP-actin with the ends of actin filaments. J. Cell Biol. 103:2747.
44. Fujiwara, I., D. Vavylonis, and T. D. Pollard, 2007. Polymerization kinetics of ADP- and ADP-Pi-actin determined by fluorescence microscopy. Proc. Natl. Acad. Sci. U. S. A. 104:8827–8832.
45. Peskin, C. S., G. M. Odell, and G. F. Oster, 1993. Cellular motions and thermal fluctuations: the Brownian ratchet. Biophys. J. 65:316–324.
46. Lipková, J., K. C. Zygalakis, S. J. Chapman, and R. Erban, 2011. Analysis of Brownian Dynamics Simulations of Reversible Bimolecular Reactions. SIAM J. Appl. Math. 71:714–730.
47. Erban, R., and S. J. Chapman, 2009. Stochastic modelling of reaction–diffusion processes: algorithms for bimolecular reactions. Phys. Biol. 6:46001.
48. Vavylonis, D., Q. Yang, and B. O'Shaughnessy, 2005. Actin polymerization kinetics, cap structure, and fluctuations. Proc. Natl. Acad. Sci. U. S. A. 102:8543–8548.
49. Carlsson, A. E., and A. E. Carlsson, 2001. Growth of Branched Actin Networks against Obstacles. Biophys. J. 81:1907–1923.
50. Lin, L. C. L., and F. L. H. Brown, 2004. Brownian dynamics in Fourier space: Membrane simulations over long length and time scales. Phys. Rev. Lett. 93:1–4.
51. Wang, R., and A. E. Carlsson, 2014. Load sharing in the growth of bundled biopolymers. New J. Phys. 16:113047.
52. Das, D., D. Das, and R. Padinhateeri, 2014. Force-induced dynamical properties of multiple cytoskeletal filaments are distinct from that of single filaments. PLoS One 9:e114014.
53. Zhuravlev, P. I., and G. A. Papoian, 2011. Protein fluxes along the filopodium as a framework for understanding the growth-retraction dynamics. Cell Adhesion & Migration 5:448–456.
54. Ester, M., H. P. Kriegel, J. Sander, and X. Xu, 1996. A Density-Based Algorithm for Discovering Clusters in Large Spatial Databases with Noise. In Second Int. Conf. Knowl. Discov. Data Min. 226–231.
55. Pedregosa, F., G. Varoquaux, A. Gramfort, V. Michel, B. Thirion, O. Grisel, M. Blondel, P. Prettenhofer, R. Weiss, V. Dubourg, J. Vanderplas, A. Passos, D. Cournapeau, M. Brucher, M. Perrot, and E. Duchesnay, 2011. Scikit-learn: Machine Learning in Python. J. Mach. Learn. Res. 12:2825–2830.
56. Zhuravlev, P. I., Y. Lan, M. S. Minakova, and G. A. Papoian, 2012. Theory of active transport in filopodia and stereocilia. Proc. Natl. Acad. Sci. 109:10849–10854.
57. Mogilner, A., and L. Edelstein-Keshet, 2002. Regulation of Actin Dynamics in Rapidly Moving Cells:A Quantitative Analysis. Biophysical Journal 83:1237 – 1258.
58. De La Cruz, E. M., E. Ostap, R. A. Brundage, K. Reddy, H. L. Sweeney, and D. Safer, 2000. Thymosin-β4 Changes the Conformation and Dynamics of Actin Monomers. Biophysical

Journal 78:2516 – 2527.

59. Landau, L. D., and E. M. Lifshitz, 1995. The Theory of Elasticity. Butterworth-Heinemann, Boston, MA.
60. Suraneni, P., B. Fogelson, B. Rubinstein, P. Noguera, N. Volkmann, D. Hanein, A. Mogilner, and R. Li, 2015. A Mechanism of Leading Edge Protrusion in the Absence of Arp2/3 Complex. Mol. Biol. Cell 26.
61. Svitkina, T. M., E. A. Bulanova, O. Y. Chaga, D. M. Vignjevic, S. ichiro Kojima, J. M. Vasiliev, and G. G. Borisy, 2003. Mechanism of filopodia initiation by reorganization of a dendritic network. J. Cell Biol. 160:409–421.
62. Miller, J., S. E. Fraser, and D. McClay, 1995. Dynamics of thin filopodia during sea urchin gastrulation. Development 121:2501–2511.
63. Khurana, S., and S. P. George, 2011. The role of actin bundling proteins in the assembly of filopodia in epithelial cells. Cell Adh. Migr. 5:409–420.
64. Grolig, F., J. Moch, A. Schneider, and P. Galland, 2014. Actin cytoskeleton and organelle movement in the sporangiophore of the zygomycete Phycomyces blakesleeanus. Plant Biol. 16:167–178.